

Supplemental Materials:

Twist Angle Dependent Interlayer Exciton Lifetimes in van der Waals Heterostructures

Junho Choi,^{1,*} Matthias Florian,^{2,*} Alexander Steinhoff,² Daniel Erben,² Kha Tran,¹ Dong Seob Kim,¹ Liuyang Sun,¹ Jiamin Quan,¹ Robert Claassen,¹ Somak Majumder,³ Jennifer A. Hollingsworth,³ Takashi Taniguchi,⁴ Kenji Watanabe,⁵ Keiji Ueno,⁶ Akshay Singh,⁷ Galan Moody,⁸ Frank Jahnke,² and Xiaoqin Li^{1,†}

¹*Department of Physics and Center for Complex Quantum Systems,
The University of Texas at Austin, Austin, TX 78712, USA.*

²*Institute for Theoretical Physics, University of Bremen, 28334 Bremen, Germany.*

³*Materials Physics & Applications Division: Center for Integrated Nanotechnologies,
Los Alamos National Laboratory, Los Alamos, New Mexico 87545, USA.*

⁴*International Center for Materials Nanoarchitectonics, National Institute for Materials Science,
1-1 Namiki, Tsukuba, Ibaraki 305-0044, Japan.*

⁵*Research Center for Functional Materials, National Institute for Materials Science,
1-1 Namiki, Tsukuba, Ibaraki 305-0044, Japan.*

⁶*Department of Chemistry, Graduate School of Science and Engineering, Saitama University, Saitama, 338-8570, Japan.*

⁷*Department of Physics, Indian Institute of Science, Bengaluru, Karnataka 560012, India.*

⁸*Department of Electrical and Computer Engineering,
University of California Santa Barbara, Santa Barbara, CA 93106, USA.*

Contents

S1. Details on sample preparation	1
S2. SHG measurements on monolayers and a twisted bilayer (TBL)	1
S3. Low-temperature photoluminescence (PL) measurements in TBLs	1
S4. Twist angle dependent moiré superlattice periodicity	2
S5. Estimation of IX quantum yield at low-temperature under non-resonant excitation	3
S6. Measured energy resolved TRPL	3
S7. Calculated moiré exciton band structure at 300 K and measured temperature dependent TRPL spectrum	3
S8. Rate equations for a three-level system including a dark exciton state	3
S9. Moiré exciton lifetime calculations	4
S10. Calculation of the dielectrically screened Coulomb potential	6
References	7

S1. Details on sample preparation

MoSe₂, WSe₂, and hexagonal boron nitride (hBN) layers were mechanically exfoliated from bulk crystals onto a polydimethylsiloxane (PDMS) sheet. The crystalline orientations of the MoSe₂ and WSe₂ monolayers were confirmed by second-harmonic generation (SHG) and rotationally aligned by high-resolution optical microscope images during the transfer. Each layer was transferred from the PDMS sheet to a targeted substrate or layer by 'stamping' dry-transfer method [1]. After

each layer was transferred, thermal annealing in a high vacuum ($\sim 10^{-6}$ mbar) at 200 °C for 6 hours was performed to reduce the polymer residue from the surface contacted to the PDMS sheet.

S2. SHG measurements on monolayers and a twisted bilayer (TBL)

The crystal orientations of MoSe₂ and WSe₂ monolayers (MLs) were determined by polarization-resolved SHG measurements. The details have been discussed in the previous studies [2–4]. Since the SHG measurements on both MoSe₂ and WSe₂ MLs exhibit a six-fold degeneracy, *R*- or *H*-stacking ($\Theta = 0^\circ$ or 60°) order of TBL region cannot be distinguished based on these measurements. In order to determine the relative twist-angle between the two MLs, SHG measurements on MoSe₂ ML, WSe₂ ML, and TBL regions were performed with a mode-locked ultrafast laser tuned to 800 nm. The SHG signals from individual MLs are expected to interfere with a relative phase difference depending on the twist-angle [5]. The SHG intensity from TBL region with *R*- (*H*-) stacking order is expected to be stronger (weaker) than ML regions. As shown in Fig. S1, the SHG signals on individual MLs show similar intensities while the SHG signal from the TBL region is enhanced compared to those from the ML regions, indicating the relative twist-angle between the MLs is near 0° stacking (or *R*-stacking).

S3. Low-temperature photoluminescence (PL) measurements in TBLs

For steady state PL measurements, a 660 nm continuous wave laser was focused to a spot size of $\sim 1 \mu\text{m}$ in diameter on the sample. The collected PL signal was guided to a spectrometer and detected by a charge-coupled device. All samples were held at ~ 13 K and an average power of 100 μW was used to acquire the PL spectrum. For time-resolved PL (TRPL) measurements, 100 fs pulses at 680 nm with a 76 Mhz repetition rate generated by a Ti:sapphire-pumped optical parametric os-

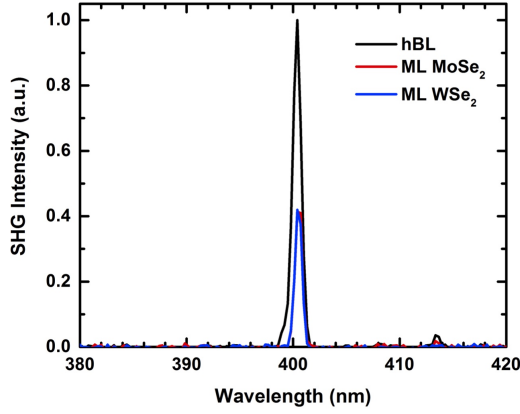


FIG. S1: SHG spectrum measured on MoSe₂ ML (red), WSe₂ ML (blue), and TBL region (black).

cillator was used as the excitation source for a $\Theta = 1.0 \pm 0.3^\circ$ TBL. For TBLs with $\Theta = 2.2 \pm 0.3^\circ$ and $3.5 \pm 0.3^\circ$, 100 fs pulses tuned to 705 nm with a 76 Mhz repetition rate first pass through a pulse picker to reduce the repetition rate in order to measure the longer lifetimes. The TRPL signal was sent through a spectrometer to select the energy of a particular interlayer exciton resonance. All TRPL measurements were performed at ~ 13 K unless stated otherwise.

The TBL with $\Theta = 1.0 \pm 0.3^\circ$ twist-angle is prepared on sapphire substrate after encapsulation by hBN. The TBLs with $2.2 \pm 0.3^\circ$ and $3.5 \pm 0.3^\circ$ twist-angle are prepared on SiO₂/Si substrate, as shown in Fig. S2. Different substrates can influence exciton resonant energy and radiative lifetime, the common bottom hBN layers reduce this dependence [6]. The thickness of all hBN layers for encapsulation is from 20 to 50 nm, providing the similar dielectric environment to all TBLs [7]. In low-temperature PL spectrum, both intra- and inter-layer exciton (IX) resonances are clearly observed in all TBLs. The microscope images and PL spectrum for the $\Theta = 1.0 \pm 0.3^\circ$ are shown in the main text while those for the other two TBLs are shown in Fig. S2. The averaged energy spacings are 21 ± 2 , 23 ± 2 , and 28 ± 3 meV for $\Theta = 1, 2.2,$ and 3.5° TBLs, respectively. The observation of larger energy spacing with increasing the twist angle is consistent with a smaller lateral size of the quantum confinement imposed by the moiré supercell. We compare the IX PL spectra from two different positions on the same TBL as shown in Fig. S2c-e, for all three TBLs. We consistently observe multiple IX resonances and the energies of IXs shift ~ 10 meV. The slight energy variation of IX resonances may be resulting from the dielectric disorder due to the residue. A similar amount of spectral shift has been reported in other experiments [6].

S4. Twist angle dependent moiré superlattice periodicity

The lattice constants of MoSe₂ and WSe₂ ($\simeq 0.1\%$) are very similar because of the common chalcogen (Se) atom. The periodicity (a_M) of moiré pattern in MoSe₂/WSe₂ TBL with a small relative twist angle (Θ) can be estimated by [8],

$$a_M \approx a_0 / \sqrt{\Theta^2 + \delta^2} \quad (1)$$

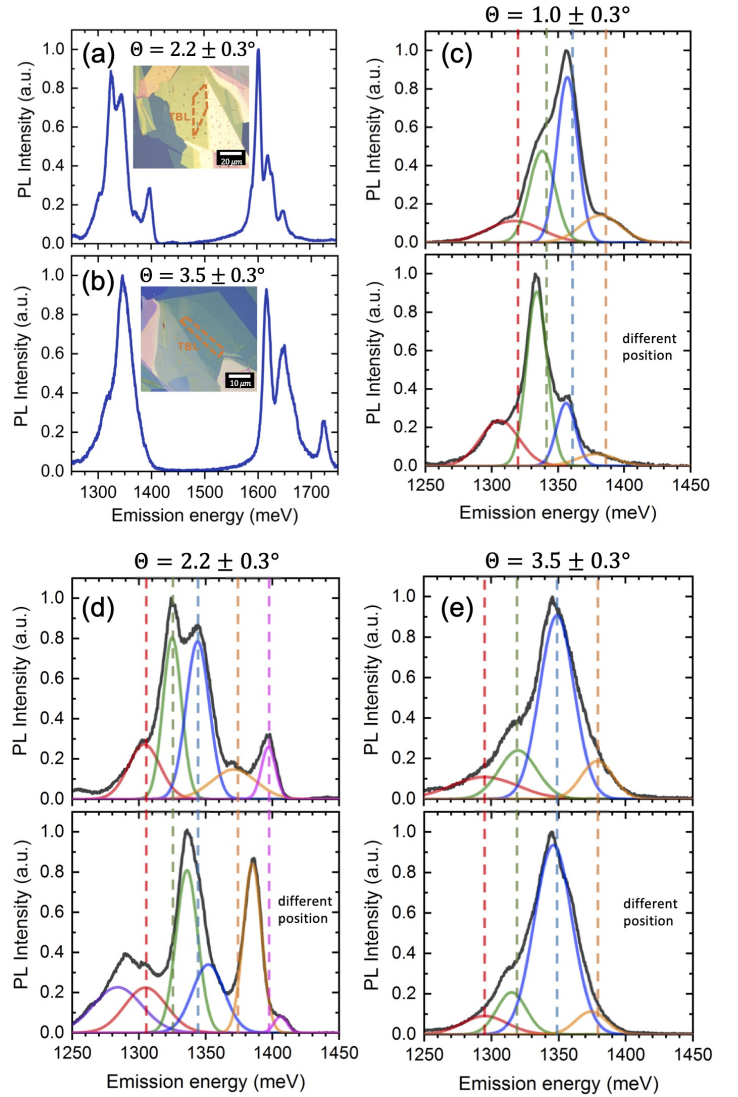


FIG. S2: Low-temperature PL spectrum of MoSe₂/WSe₂ TBLs and IX PL spectrum from different positions. (a, b) Low-temperature PL spectrum from hBN-encapsulated MoSe₂/WSe₂ TBLs with $\Theta = 2.2 \pm 0.3^\circ$ and $3.5 \pm 0.3^\circ$ twist angles over a broad spectral range to include both intra- and inter-layer excitons. Inset shows the optical image of the TBL with a scale bar and the TBL region is indicated with the orange dashed line. (c-e) Gaussian fitting to multiple IX resonances in the TBLs with three different twist angles and from two different positions on each sample TBL. Black solid line is the measured PL spectrum.

where the lattice mismatch ($\delta = |a_0 - a'_0|/a_0$) is given by the lattice constants of two MLs (a_0 and a'_0). For TBLs with $\Theta = 1^\circ - 3.5^\circ$, the contribution of δ is negligible. In other words, the moiré superlattice periodicity is primarily controlled by the twist angle between the two MLs. The moiré periodicity is changed from 18.9 to 5.4 nm when the twist-angle is changed from 1° to 3.5° , as shown in Fig. S3.

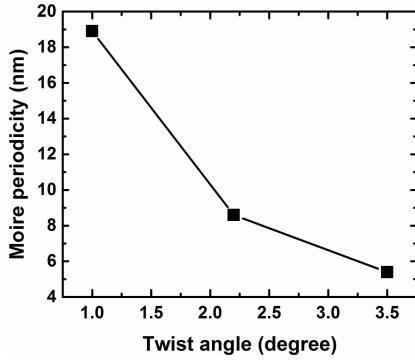


FIG. S3: Twist angle dependent moiré periodicity of the TBLs with $\Theta = 1^\circ$ to 3.5° .

S5. Estimation of IX quantum yield at low-temperature under non-resonant excitation

Under resonant excitation conditions, the quantum yield (η) of a two-level emitter can be defined in terms of radiative decay (γ_{rad}) and non-radiative decay (γ_{nrad}) rates according to the relation, $\eta = \gamma_{rad}/(\gamma_{rad} + \gamma_{nrad}) = \tau_{total}/\tau_{rad}$ where the total decay rate is defined as $\gamma_{total} = \gamma_{rad} + \gamma_{nrad} = 1/\tau_{total}$.

It is extremely challenging to obtain such measurements for the IXs because of the small dipole moments and weak absorption. We measured the relative PL quantum yield (QY) of IXs under non-resonant excitation conditions, which serves to provide an empirical guidance of the expected PL signal. We used a thin film of diluted colloidal CdSe/CdS core/shell quantum dots (QDs), comprising an ultra-thick CdS shell (~ 16 monolayers), with near 50% QY as a calibration sample [9, 10]. We used spin coating to prepare multiple films with different concentrations of diluted QD solution and measured the absorption and PL under the same experimental conditions. The area of PL spectrum was integrated to count the total number of emitted photons. We confirm that there is linear relation between the PL counts as a function of absorbance, indicating no re-absorption effect of emitted photons in the calibration samples, as expected for the thick-shell QDs for which the predominant absorption onset occurs above 2.4 eV; whereas, emission is at ~ 1.9 eV [11]. The TBL with $\Theta = 2.2 \pm 0.3^\circ$ twist-angle was chosen as a representative sample and the QY at low-temperature was estimated to be $\simeq 0.1\%$. This relatively low QY under the non-resonant excitation conditions can be attributed to different decay channels including the population of dark states, an efficient radiative decay of the intralayer excitons, and phonon assisted non-radiative decays.

S6. Measured energy resolved TRPL

Emission energy resolved TRPL measured from three different twist angles are presented in Fig. S4. We include all interlayer exciton resonances here. For all IX resonances, we observe the consistent trend that a longer IX lifetime is found in a TBL with a larger twist angle than that in a TBL with a smaller twist angle.

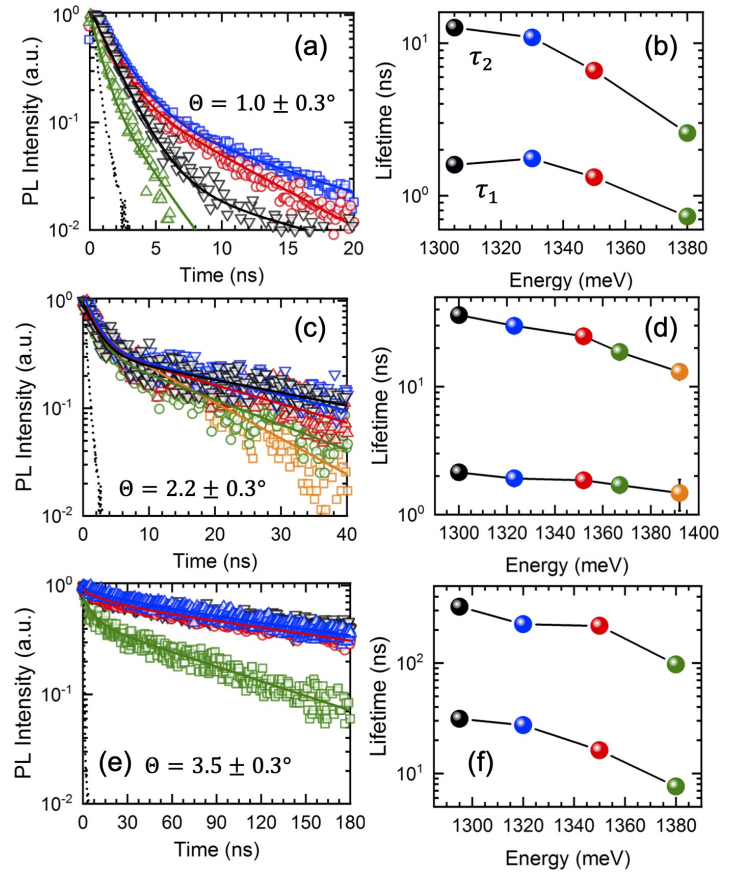


FIG. S4: Emission energy resolved TRPL in TBLs with (a) $\Theta = 1.0 \pm 0.3^\circ$, (c) $2.2 \pm 0.3^\circ$, and (e) $3.5 \pm 0.3^\circ$. (b, d, f) Fast (τ_1) and slow (τ_2) component of IX lifetime extracted by fitting with biexponential function for TBL with these three different twist angles.

S7. Calculated moiré exciton band structure at 300 K and measured temperature dependent TRPL spectrum

Figure S5 shows the IX band structure in the presence of moiré potential at 300 K and temperature dependent TRPL spectrum from TBLs with two different twist angles. We observe that the thermally broadened IX distribution leads to a significantly stronger exciton-photon coupling at large twist angles compared to the low-temperature results shown in Fig. 4 in the main text.

S8. Rate equations for a three-level system including a dark exciton state

To describe the biexponential decay observed, we model the decay dynamics of a three-level system consisting of the bright exciton, dark exciton, and crystal ground state, often used in modeling semiconductor nanostructures [12]. The relevant dynamic parameters include the bright exciton radiative decay rate (γ_{Br}), non-radiative decay rates (γ_{Bnr} and γ_{Dnr}), and conversion rates between the bright and dark exciton states

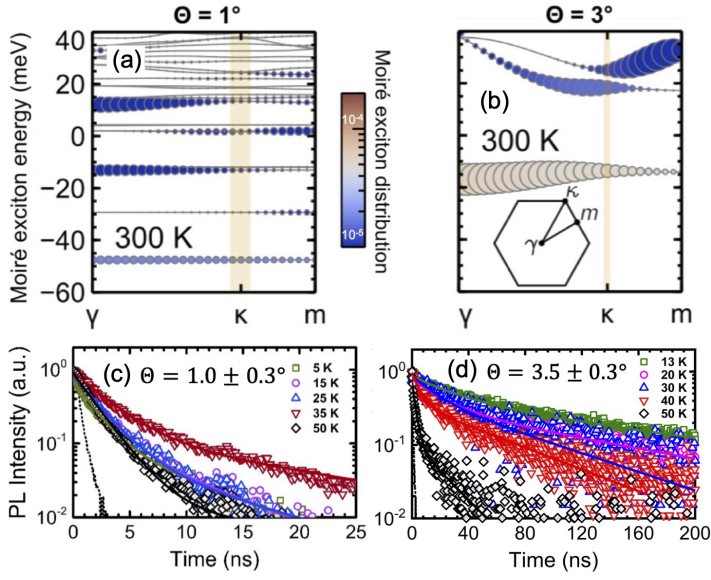


FIG. S5: Moiré exciton band structure at 300 K in TBLs with twist angles of (a) $\Theta = 1^\circ$ and (b) $\Theta = 3^\circ$, respectively. Inset in panel (b) illustrates the first moiré Brillouin zone (MBZ). The scale of the symbol size and color scale are the same as Fig. 4 in the main text. Panels (c) and (d) show temperature dependent TRPL spectrum from TBLs with $\Theta = 1.0 \pm 0.3^\circ$ and $3.5 \pm 0.3^\circ$.

(γ_{BD} and γ_{DB}), as shown in Fig. S6. The rate equations are

$$\begin{aligned} \frac{dn_B}{dt} &= -n_B(\gamma_{Br} + \gamma_{Bnr} + \gamma_{BD}) + n_D\gamma_{DB}, \\ \frac{dn_D}{dt} &= -n_D(\gamma_{Dnr} + \gamma_{DB}) + n_B\gamma_{BD}, \end{aligned} \quad (2)$$

where n_B and n_D are occupations in the bright and dark state, respectively. The solution of the rate equations is a biexponential decay function, $n_B(t) = a_1 e^{-\gamma_1 t} + a_2 e^{-\gamma_2 t}$, with the fast and slow decay components

$$\begin{aligned} \gamma_{1,2} &= \frac{1}{2}(\gamma_{Br} + \gamma_{Bnr} + \gamma_{Dnr} + \gamma_{BD} + \gamma_{DB}) \\ &\pm \frac{1}{2}\sqrt{(\gamma_{Br} + \gamma_{Bnr} + \gamma_{Dnr} + \gamma_{BD} + \gamma_{DB})^2} \\ &- 4\gamma_r(\gamma_{Dnr} + \gamma_{DB}) - 4(\gamma_{Bnr}\gamma_{Dnr} + \gamma_{BD}\gamma_{Dnr} + \gamma_{DB}\gamma_{Bnr}). \end{aligned} \quad (3)$$

In the case of $\gamma_{Br} \gg \gamma_{BD}, \gamma_{DB}$, the fast and slow decay rates can be approximated as

$$\begin{aligned} \gamma_1 &\simeq \gamma_{Br} + \gamma_{Bnr} + \gamma_{BD}, \\ \gamma_2 &\simeq \gamma_{Dnr} + \gamma_{DB}. \end{aligned} \quad (4)$$

Using γ_1 ($= 1/\tau_1$) and γ_2 ($= 1/\tau_2$) to represent the fast and slow decay component, this model may be used to explain the biexponential decay observed in our TRPL experiments by attributing the fast (slow) decay component to the bright (dark) exciton lifetime.

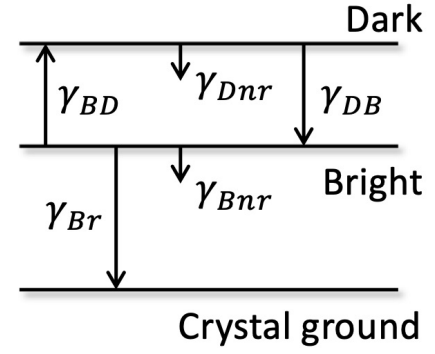


FIG. S6: Schematic of three level systems: dark exciton, bright exciton, and crystal ground state. The bright exciton can radiatively decay (γ_{Br}) and both bright and dark excitons can non-radiatively decay (γ_{Bnr} and γ_{Dnr}). The bright and dark exciton states can be converted (γ_{BD} and γ_{DB}) to the other state via thermal or valley scattering processes.

S9. Moiré exciton lifetime calculations

The radiative moiré exciton recombination rate is calculated using the Fermi's golden rule [13]

$$\tau_{IX}^{-1} = \frac{2\pi}{\hbar} \sum_{if} |\langle f | H_{\text{rad}} | i \rangle|^2 \delta(\varepsilon_i - \varepsilon_f) N_i \quad (5)$$

where the optical matrix element describes transitions between the initial exciton state $|i\rangle$ and the final photon state $|f\rangle = b_{\mathbf{q},\sigma}^\dagger |0\rangle$. Here, $b_{\mathbf{q},\sigma}^\dagger$ creates a photon with wave vector \mathbf{q} and polarization σ with respect to the vacuum state $|0\rangle$. N_i is the occupation of the initial exciton states.

Under weak excitation conditions and using the Coulomb-gauge the light-matter interaction can be written as

$$\begin{aligned} H_{\text{rad}} &= \frac{1}{c} \sum_{\mathbf{R}\mathbf{R}'\nu\nu'} \mathbf{A} \left(\frac{\mathbf{R} + \mathbf{R}'}{2} \right) a_{\mathbf{R}}^{\dagger,\nu} a_{\mathbf{R}'}^{\nu'} \times \\ &\times \int d^3r u_\nu^*(\mathbf{r} - \mathbf{R}) \mathbf{j} u_{\nu'}(\mathbf{r} - \mathbf{R}'), \end{aligned} \quad (6)$$

where $a_{\mathbf{R}}^{\dagger,\nu}$ creates an electron at lattice site \mathbf{R} in band ν . To obtain eq. (6), we have assumed that the Wannier functions $u_{\nu\sigma}(\mathbf{r} - \mathbf{R})$ are localized at the lattice sites and that the vector potential $\mathbf{A}(\mathbf{R})$ is slowly varying over the unit cell.

The vector potential is expanded into a plane-wave basis

$$\mathbf{A}(\mathbf{R}) = \sum_{\mathbf{q}\sigma} \sqrt{\frac{2\pi\hbar c}{n^2 q \Omega}} \mathbf{e}_{\mathbf{q}\sigma} \left(b_{\mathbf{q},\sigma} e^{i\mathbf{q}\parallel\mathbf{R}} + b_{-\mathbf{q},\sigma}^\dagger e^{-i\mathbf{q}\parallel\mathbf{R}} \right), \quad (7)$$

where Ω is the normalization volume of the photon eigenmodes, $\mathbf{e}_{\mathbf{q}\sigma}$ are the unit vectors of the two transversal photon polarizations and n is the average refractive index of the dielectric environment of the heterobilayer. For the optical matrix element in eq. (6) we use the two-center approximation [14]. As a result the matrix element

$$\int d^3r u_\nu^*(\mathbf{r} - \mathbf{R}) \mathbf{j} u_{\nu'}(\mathbf{r} - \mathbf{R}') \approx \mathbf{j}_{\nu\nu'}(\mathbf{R} - \mathbf{R}') \quad (8)$$

depends only on the difference between the electron and hole

position and can be expressed in terms of its Fourier transform

$$\mathbf{j}_{\nu\nu'}(\mathbf{R} - \mathbf{R}') = \frac{1}{N} \sum_{\mathbf{q}} e^{-i\mathbf{q}(\mathbf{R}-\mathbf{R}')} \mathbf{j}_{\nu\nu'}(\mathbf{q}), \quad (9)$$

where N is the number of unit cells in each layer.

To describe the moiré exciton states we use a low energy continuum model that we derive along the lines of Ref. [8, 15–17]. For each monolayer the band edge electrons and holes at the K point are predominantly described by Wannier functions of the metal d-orbitals [18]. In the absence of interlayer hybridization, the IX is described by the wave function

$$|\mathbf{Q}\rangle = \frac{1}{\sqrt{\mathcal{A}}} \sum_{\mathbf{k}} \phi_X(\mathbf{k}) a_{\mathbf{K}_c+\mathbf{k}+\frac{m_e}{M}\mathbf{Q}}^{\dagger,c} a_{\mathbf{K}_v+\mathbf{k}-\frac{m_h}{M}\mathbf{Q}}^v |0\rangle \quad (10)$$

with eigenenergies $E(\mathbf{Q}) = \hbar^2|\mathbf{Q}|^2/(2M) + E_{\text{gap}} - E_B$ that are characterized by the center-of-mass momentum \mathbf{Q} , $M = m_e + m_h$ is the total exciton mass, and m_e (m_h) is the electron (hole) effective mass. \mathcal{A} is the crystal area. The operator $a_{\mathbf{K}_c+\mathbf{q}}^{\dagger,c}$ ($a_{\mathbf{K}_v+\mathbf{q}}^v$) creates (annihilates) an electron in the \mathbf{K}_c (\mathbf{K}_v)-valley of the conduction (valence) band and can be expanded in terms of their Wannier counterparts

$$a_{\mathbf{q}}^{\dagger,c} = \frac{1}{\sqrt{N}} \sum_{\mathbf{R}} e^{i\mathbf{q}\mathbf{R}} a_{\mathbf{R}}^c \quad \text{and} \quad a_{\mathbf{q}}^v = \frac{1}{\sqrt{N}} \sum_{\mathbf{R}} e^{-i\mathbf{q}\mathbf{R}} a_{\mathbf{R}}^v \quad (11)$$

The electron-hole relative-motion wave function in momentum space $\phi_X(\mathbf{k})$ is determined by the Wannier equation

$$\sum_{\mathbf{q}'} \left[\frac{\hbar^2 \mathbf{q}^2}{2\mu} \delta_{\mathbf{q}\mathbf{q}'} - \frac{1}{\mathcal{A}} V_{|\mathbf{q}-\mathbf{q}'|} \right] \phi_X(\mathbf{q}') = -E_B \phi_X(\mathbf{q}) \quad (12)$$

where $\mu = m_e m_h / (m_e + m_h)$ is the reduced mass. The solution of eq.(12) determines the exciton energy $E_{\text{gap}} - E_B$, where E_B is the exciton binding energy and E_{gap} the band gap. For the effective masses we use $m_e = 0.57m_0$ and $m_h = 0.36m_0$, where m_0 is the free electron mass. [19] Details about the dielectrically screened Coulomb potential are given in (S7). We find that the IX binding energy E_B for the hBN-encapsulated MoSe₂/WSe₂ heterobilayer is about 110 meV. The exciton Bohr radius a_B can be approximated by the root mean square of the electron hole separation and we obtain a value of 1.15 nm.

An interlayer twist in real space generates a relative shift in momentum space ($\mathbf{K}_c - \mathbf{K}_v$) as well as a spatial modulation of the exciton energy. For small twist angle, the moiré periodicity can be assumed to be large compared to the exciton Bohr radius. Thus, we neglect the variation of the binding energy in the moiré pattern and use a local approximation of the exciton moiré potential $V^M(\mathbf{R})$ according to Ref. [8]. In this framework, the exciton Hamiltonian reads

$$H = -\frac{\hbar^2}{2M} \Delta_{\mathbf{R}} + V^M(\mathbf{R}) \quad (13)$$

and can be diagonalized using a plane-wave expansion

$$\left[\frac{\hbar^2}{2M} (\mathbf{Q} - \mathbf{G}_M)^2 - \varepsilon_{\mathbf{Q},\lambda} \right] c_{\mathbf{Q}-\mathbf{G}_M}^{\lambda} \delta_{\mathbf{G}_M, \mathbf{G}'_M} + \sum_{\mathbf{G}'_M} V_{\mathbf{G}_M, \mathbf{G}'_M}^M c_{\mathbf{Q}-\mathbf{G}'_M}^{\lambda} = 0 \quad (14)$$

with eigenenergies $\varepsilon_{\mathbf{Q},\lambda}$ and eigenstates

$$|\mathbf{Q}, \lambda\rangle = \sum_{\mathbf{G}_M} c_{\mathbf{Q}-\mathbf{G}_M}^{\lambda} |\mathbf{Q} - \mathbf{G}_M\rangle. \quad (15)$$

The moiré reciprocal lattice vectors \mathbf{G}_M are derived as differences of top and bottom layer reciprocal lattice vectors. Therefore, the size of the MBZ scales with the interlayer twist angle. Following Ref. [8] the moiré potential can be parameterized according to

$$V^M(\mathbf{R}) \approx \sum_{j=1}^6 V_j e^{i\mathbf{G}_{M,j}\mathbf{R}}, \quad (16)$$

where the Fourier series is restricted to the first shell of reciprocal Moire lattice vectors $\mathbf{G}_{M,j}$. Due to \hat{C}_3 symmetry $V_1 = V_3 = V_5$, as well as $V_2 = V_4 = V_6$. Because $V^M(\mathbf{R})$ is real, $V_1 = V_4^* \equiv V \exp(-i\psi)$. For the parameter (V, ψ) we use (11.8, 79.5°) as obtained from DFT calculations for AA stacked MoSe₂/WSe₂ heterobilayer [8].

Using the above plane-wave expansion, the optical matrix element between the initial moiré exciton state $|\mathbf{Q}, \lambda\rangle$ and the final photon state $|\mathbf{q}, \sigma\rangle$ can be expressed as:

$$\begin{aligned} \langle \mathbf{q}, \sigma | H_{\text{rad}} | \mathbf{Q}, \lambda \rangle &= \sqrt{\frac{2\pi\hbar}{cn^2|\mathbf{q}|\Omega}} \phi_X(\mathbf{r}=0) \sum_{\mathbf{G}_M, \mathbf{G}_c, \mathbf{G}_v} c_{\mathbf{Q}+\mathbf{G}_M}^{\lambda} \times \\ &\times \mathbf{j}_{\text{vc}} \left((\mathbf{K}_v + \mathbf{G}_v) - \frac{m_h}{M} (\mathbf{Q} - \mathbf{G}_M) + \frac{\mathbf{q}_{\parallel}}{2} \right) \cdot \mathbf{e}_{\mathbf{q}\sigma} \times \\ &\times \delta_{\mathbf{Q}-\mathbf{G}_M, (\mathbf{K}_c+\mathbf{G}_c)-(\mathbf{K}_v+\mathbf{G}_v)+\mathbf{q}_{\parallel}}. \end{aligned} \quad (17)$$

Here, the interlayer current matrix element $\mathbf{j}_{\text{vc}}(\mathbf{Q})$ is expected to rapidly decline on the scale of the monolayer lattice vector [8]. We assume that the twist angle is sufficiently large so that typical photon momenta are still small compared to the MBZ, which in our case is well-justified for twist angles larger than 0.5°. In this case, umklapp processes can be discarded. As a result, moiré excitons can only recombine if the momentum conservation law $\mathbf{Q} - \mathbf{q}_{\parallel} = \mathbf{K}_c - \mathbf{K}_v := \kappa$ is fulfilled where \mathbf{q}_{\parallel} represents the in-plane component of the photon wave vector. Under these assumptions the optical matrix element reads

$$\begin{aligned} \langle \mathbf{q}, \sigma | H_{\text{rad}} | \mathbf{Q}, \lambda \rangle &\approx \sqrt{\frac{2\pi\hbar}{cn^2|\mathbf{q}|\Omega}} \phi_X(\mathbf{r}=0) c_{\mathbf{Q}}^{\lambda} \times \\ &\times \mathbf{j}_{\text{vc}} \cdot \mathbf{e}_{\mathbf{q}\sigma} \delta_{\mathbf{Q}, \mathbf{K}_c - \mathbf{K}_v + \mathbf{q}_{\parallel}} \delta_{\mathbf{G}_M, 0}, \end{aligned} \quad (18)$$

where $\mathbf{j}_{\text{vc}} = \langle v\mathbf{K} | \mathbf{j} | c\mathbf{K} \rangle$ is the interlayer current matrix element of the untwisted heterobilayer. Optical transitions at the \mathbf{K} point satisfy circular polarization selection rules with matrix elements $|\mathbf{j}_{\text{vc}} \cdot \mathbf{e}_{\pm}^+|/\mathcal{D} = 0.22$ and $|\mathbf{j}_{\text{vc}} \cdot \mathbf{e}_{\pm}^-|/\mathcal{D} = 0.06$, where $\mathbf{e}_{\pm} = (1, \pm i)/\sqrt{2}$ and $\hbar/e\mathcal{D} = 4.43$ eV Å. [8]. We neglect the significantly weaker transition with \mathbf{e}_{-} polarization direction.

We decompose the photon wave vector into the in- and out-of-plane components as $\mathbf{q} = \{\mathbf{q}_{\parallel}, q_z\}$ such that the summation over q_z in Eq. (5) yields the one-dimensional density-of-states and gives rise to radiative decay of excitons with wave vectors inside the light cone $|\kappa| - q_{\lambda} < |\mathbf{Q}| < |\kappa| + q_{\lambda}$. The boundary of the light cone is determined by the photon dispersion $\hbar c q_{\lambda} = n \varepsilon_{\kappa, \lambda}$. Combining eqs. (5) and (17) we finally obtain for the

moiré exciton lifetime

$$\tau_{\text{IX}}^{-1} = \frac{2\pi}{\hbar c^2} g^{\text{rad}} |\phi_X(\mathbf{r}=0)|^2 \sum_{\lambda} \int \frac{d^2 \mathbf{q}_{\parallel}}{(2\pi)^2} \left| j_{\text{vc}} c_{\kappa+\mathbf{q}_{\parallel}}^{\lambda} \right|^2 N_{\kappa+\mathbf{q}_{\parallel}}^{\lambda} \times \frac{1}{q_{\lambda}} \left\{ \frac{1}{\sqrt{1 - (q_{\parallel}/q_{\lambda})^2}} - \sqrt{1 - (q_{\parallel}/q_{\lambda})^2} \right\} \Theta(q_{\lambda} - q_{\parallel}). \quad (19)$$

Here, g^{rad} is the degeneracy of optically active exciton states and accounts for time-reversal symmetry. The moiré exciton distribution $N_{\mathbf{Q}}^{\lambda}$ is assumed to be thermalized obeying a Boltzmann distribution. We consider the low density limit such that the exciton distribution is normalized to unit total density, $g_X \sum_{\mathbf{Q}, \lambda} N_{\mathbf{Q}}^{\lambda} = 1$, where g_X denotes the degeneracy of occupied (bright and dark) exciton states. In particular, in the limit of zero twist-angle eq. (19) recovers the result of Esser et al. [13] that has been previously derived for quantum well excitons.

S10. Calculation of the dielectrically screened Coulomb potential

We start by introducing the static nonlocal charge-density susceptibility $\chi(\mathbf{r}, \mathbf{r}') = \chi(\mathbf{r}, \mathbf{r}', \omega = 0)$ that connects the material polarization $\mathbf{P}(\mathbf{r})$ to the electric field $\mathbf{E}(\mathbf{r})$ via

$$\mathbf{P}(\mathbf{r}) = \varepsilon_0 \int d^3 \mathbf{r}' \chi(\mathbf{r}, \mathbf{r}') \mathbf{E}(\mathbf{r}'). \quad (20)$$

The polarization is also related to the induced charge density $\rho_{\text{ind}}(\mathbf{r})$ via

$$\nabla_{\mathbf{r}} \cdot \mathbf{P}(\mathbf{r}) = -\rho_{\text{ind}}(\mathbf{r}). \quad (21)$$

The total charge density can be expressed as a sum of free and induced charges:

$$\rho(\mathbf{r}) = \rho_{\text{free}}(\mathbf{r}) + \rho_{\text{ind}}(\mathbf{r}). \quad (22)$$

Using Gauss's law

$$\nabla_{\mathbf{r}} \cdot \mathbf{E}(\mathbf{r}) = -\frac{\rho(\mathbf{r})}{\varepsilon_0}, \quad (23)$$

we find

$$\begin{aligned} \varepsilon_0^{-1} \rho_{\text{free}}(\mathbf{r}) &= \varepsilon_0^{-1} (\rho(\mathbf{r}) - \rho_{\text{ind}}(\mathbf{r})) \\ &= \nabla_{\mathbf{r}} \cdot \mathbf{E}(\mathbf{r}) + \varepsilon_0^{-1} \nabla_{\mathbf{r}} \cdot \mathbf{P}(\mathbf{r}) \\ &= \nabla_{\mathbf{r}} \cdot \left(\mathbf{E}(\mathbf{r}) + \int d^3 \mathbf{r}' \chi(\mathbf{r}, \mathbf{r}') \mathbf{E}(\mathbf{r}') \right) \\ &= \nabla_{\mathbf{r}} \cdot \int d^3 \mathbf{r}' \varepsilon_r(\mathbf{r}, \mathbf{r}') \mathbf{E}(\mathbf{r}'), \end{aligned} \quad (24)$$

where we introduced the dielectric function

$$\varepsilon_r(\mathbf{r}, \mathbf{r}') = \delta(\mathbf{r} - \mathbf{r}') + \chi(\mathbf{r}, \mathbf{r}'). \quad (25)$$

With the effective electrostatic potential $\phi(\mathbf{r})$ given by

$$\mathbf{E}(\mathbf{r}) = -\nabla_{\mathbf{r}} \phi(\mathbf{r}), \quad (26)$$

a generalized form of Poisson's equation is derived:

$$\nabla_{\mathbf{r}} \cdot \int d^3 \mathbf{r}' \varepsilon_r(\mathbf{r}, \mathbf{r}') \nabla_{\mathbf{r}'} \phi(\mathbf{r}') = -\frac{\rho_{\text{free}}(\mathbf{r})}{\varepsilon_0}. \quad (27)$$

It yields the electrostatic potential ϕ for a given charge density ρ_{free} in the presence of a dielectric function ε_r describing nonlocal screening effects.

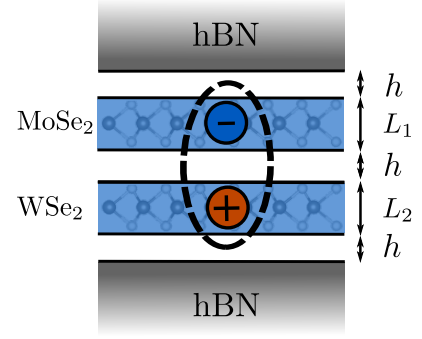


FIG. S7: Dielectric structure model for the interlayer Coulomb interaction.

We consider a dielectric heterostructure as schematically shown in Fig. S7, where the hetero-bilayer extends in the x-y plane. Making use of the in-plane homogeneity of the continuum medium, Fourier transform with respect to in-plane coordinates yields a differential equation in the z coordinate only:

$$\begin{aligned} \int dz' \left(\frac{\partial}{\partial z} \varepsilon(q, z, z') \frac{\partial}{\partial z'} \phi(q, z') - q^2 \varepsilon(q, z, z') \phi(q, z') \right) \\ = \frac{\rho_{\text{free}}(q, z)}{\varepsilon_0}. \end{aligned} \quad (28)$$

In the given geometry, where free charges can be located in different layers, nonlocality of the dielectric response, i.e. dependence of ε on two different spatial coordinates, has to be considered. We simplify the spatial dependence of ε by assuming that the hetero-bilayer can be approximated as an effective single layer with thickness $L = L_1 + L_2 + h$ and an averaged dielectric constant $\varepsilon_{\text{BL}} = (\varepsilon_{\text{MoSe}_2} L_1 + \varepsilon_{\text{WSe}_2} L_2 + h) / L$. We further assume that the dielectric function of each layer is constant and local in z direction, i.e. $\varepsilon_r(q, z, z') = \varepsilon_r(q) \delta(z - z')$. Then Poisson's equation can be solved analytically as shown in Ref. [20] to obtain the macroscopic dielectric function $\varepsilon_q = \varepsilon_r(q)$. An alternative approach to construct a dielectric function that is local in z-direction has been shown in Refs. [21, 22].

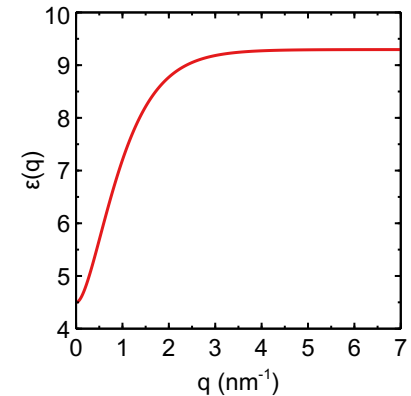


FIG. S8: Calculated macroscopic dielectric function of the dielectric heterostructure shown in Fig. S7.

The Coulomb interaction between carriers located in dif-

ferent TMD layers is weaker than the intralayer Coulomb interaction due to the spatial separation of carriers in growth (z -)direction. To account for this effect the Coulomb matrix elements V_q are modeled by using a formfactor F_q in addition to the macroscopic dielectric function ε_q according to

$$V_q = \frac{e^2}{2\varepsilon_0 q} \varepsilon_q^{-1} F_q. \quad (29)$$

The dielectric constants of the TMD materials are computed as geometric mean of the values given in [23], where also layer widths are provided. The dielectric constant of hBN is taken from [24]. The interlayer distance $h = 0.3$ nm has been found to be an appropriate value in [20]. The calculated dielectric function for dielectric heterostructure is shown in Fig. S8. In the limit of small q the dielectric function ε_q resembles the Rytova-Keldysh limit [25, 26]. Small deviations from the linear behavior arise from the interlayer distance of several Å between TMD and the hBN layers [20]. The form factor accounts for the confinement of carriers inside the atomically thin layers via the confinement functions $\xi(z)$

$$F_q = \int dz \int dz' \xi(z) \xi(z') e^{-iq|z-z'|} \xi(z') \xi(z). \quad (30)$$

For the confinement functions, we assume eigenfunctions of the infinitely deep potential well with two nodes due to the mostly d-like character of electronic orbitals, which explicitly reads

$$F_q = \frac{4}{L_1 L_2} \frac{324\pi^4 e^{-(h+L_1+L_2)q} (e^{L_1 q} - 1)(e^{L_2 q} - 1)}{q^2 [36\pi^2 + (L_1)^2 q^2] [36\pi^2 + (L_2)^2 q^2]}. \quad (31)$$

* J.C. and M.F. contributed equally to this work.

† Corresponding author; elaineli@physics.utexas.edu

- [1] A. Castellanos-Gomez, M. Buscema, R. Molenaar, V. Singh, L. Janssen, H. S. J. van der Zant, and G. A. Steele, *2D Materials* **1**, 011002 (2014).
- [2] N. Kumar, S. Najmaei, Q. Cui, F. Ceballos, P. M. Ajayan, J. Lou, and H. Zhao, *Physical Review B* **87**, 161403 (2013).
- [3] L. M. Malard, T. V. Alencar, A. P. M. Barboza, K. F. Mak, and A. M. de Paula, *Physical Review B* **87**, 201401 (2013).
- [4] Y. Li, Y. Rao, K. F. Mak, Y. You, S. Wang, C. R. Dean, and T. F. Heinz, *Nano Letters* **13**, 3329 (2013).
- [5] W. T. Hsu, Z. A. Zhao, L. J. Li, C. H. Chen, M. H. Chiu, P. S. Chang, Y. C. Chou, and W. H. Chang, *ACS Nano* **8**, 2951 (2014).
- [6] A. Raja, L. Waldecker, J. Zipfel, Y. Cho, S. Brem, J. D. Ziegler,

- M. Kulig, T. Taniguchi, K. Watanabe, E. Malic, T. F. Heinz, T. C. Berkelbach, and A. Chernikov, *Nature Nanotechnology* **14**, 832 (2019).
- [7] I. C. Gerber and X. Marie, *Physical Review B* **98**, 245126 (2018).
- [8] F. C. Wu, T. Lovorn, and A. H. MacDonald, *Physical Review B* **97**, 035306 (2018).
- [9] Y. Chen, J. Vela, H. Htoon, J. L. Casson, D. J. Werder, D. A. Bussian, V. I. Klimov, and J. A. Hollingsworth, *Journal of the American Chemical Society* **130**, 5026 (2008).
- [10] N. J. Orfield, S. Majumder, J. R. McBride, F. Yik-Ching Koh, A. Singh, S. J. Bouquin, J. L. Casson, A. D. Johnson, L. Sun, X. Li, C.-K. Shih, S. J. Rosenthal, J. A. Hollingsworth, and H. Htoon, *ACS Nano* **12**, 4206 (2018).
- [11] C. J. Hanson, M. R. Buck, K. Acharya, J. A. Torres, J. Kundu, X. Ma, S. Bouquin, C. E. Hamilton, H. Htoon, and J. A. Hollingsworth, *ACS Applied Materials & Interfaces* **7**, 13125 (2015).
- [12] P. A. Dalgarno, J. M. Smith, B. D. Gerardot, A. O. Govorov, K. Karrai, P. M. Petroff, and R. J. Warburton, *physica status solidi (a)* **202**, 2591 (2005).
- [13] A. Esser, E. Runge, R. Zimmermann, and W. Langbein, *Physical Review B* **62**, 8232 (2000).
- [14] R. Bistritzer and A. H. MacDonald, *Proceedings of the National Academy of Sciences* **108**, 12233 (2011), ISBN: 9781108174107 Publisher: National Academy of Sciences Section: Physical Sciences PMID: 21730173.
- [15] H. Yu, Y. Wang, Q. Tong, X. Xu, and W. Yao, *Physical Review Letters* **115**, 187002 (2015).
- [16] F. Wu, T. Lovorn, and A. MacDonald, *Physical Review Letters* **118**, 147401 (2017).
- [17] H. Yu, G.-B. Liu, J. Tang, X. Xu, and W. Yao, *Science Advances* **3**, e1701696 (2017).
- [18] G.-B. Liu, W.-Y. Shan, Y. Yao, W. Yao, and D. Xiao, *Physical Review B* **88**, 085433 (2013).
- [19] J. Wang, J. Ardelean, Y. Bai, A. Steinhoff, M. Florian, F. Jahnke, X. Xu, M. Kira, J. Hone, and X.-Y. Zhu, *Science Advances* **5**, eaax0145 (2019), publisher: American Association for the Advancement of Science Section: Research Article.
- [20] M. Florian, M. Hartmann, A. Steinhoff, J. Klein, A. W. Holleitner, J. J. Finley, T. O. Wehling, M. Kaniber, and C. Gies, *Nano Letters* **18**, 2725 (2018).
- [21] N. A. Asriyan, I. L. Kurbakov, A. K. Fedorov, and Y. E. Lozovik, *Physical Review B* **99**, 085108 (2019), publisher: American Physical Society.
- [22] M. A. Semina, *Physics of the Solid State* **61**, 2218 (2019).
- [23] I. Kylänpää and H.-P. Komsa, *Physical Review B* **92**, 205418 (2015).
- [24] R. Geick, C. H. Perry, and G. Rupprecht, *Physical Review* **146**, 543 (1966).
- [25] N. S. Rytova, *Proc. MSU, Phys.* **3**, 30 (1967).
- [26] L. V. Keldysh, *Soviet Journal of Experimental and Theoretical Physics Letters* **29**, 658 (1979).